

# Chemical Science

Accepted Manuscript

This article can be cited before page numbers have been issued, to do this please use: X. He, D. Xiong, K. Zhang, W. Wang, S. Xue, J. Wang, D. Wu and Z. Chen, *Chem. Sci.*, 2026, DOI: 10.1039/D5SC09133K.



This is an Accepted Manuscript, which has been through the Royal Society of Chemistry peer review process and has been accepted for publication.

Accepted Manuscripts are published online shortly after acceptance, before technical editing, formatting and proof reading. Using this free service, authors can make their results available to the community, in citable form, before we publish the edited article. We will replace this Accepted Manuscript with the edited and formatted Advance Article as soon as it is available.

You can find more information about Accepted Manuscripts in the [Information for Authors](#).

Please note that technical editing may introduce minor changes to the text and/or graphics, which may alter content. The journal's standard [Terms & Conditions](#) and the [Ethical guidelines](#) still apply. In no event shall the Royal Society of Chemistry be held responsible for any errors or omissions in this Accepted Manuscript or any consequences arising from the use of any information it contains.

# Beyond Active Sites: Interfacial Water Engineering with Single-Atom Ni-WC<sub>x</sub> for Concurrent Energy Storage and Biomass Conversion

*Xiaoyang He<sup>1</sup>, Dengke Xiong<sup>1</sup>, Kaiyan Zhang<sup>2</sup>, Wei Wang<sup>1</sup>, Shujie Xue<sup>1</sup>, Jianying Wang<sup>1,\*</sup>, Deli Wu<sup>3</sup>, and Zuofeng Chen<sup>1,\*</sup>*

<sup>1</sup>School of Chemical Science and Engineering, Tongji University, 1239 Siping Road, Shanghai 200092, China;

<sup>2</sup>Department of Chemical and Biomolecular Engineering and Ralph O'Connor Sustainable Energy Institute, Johns Hopkins University, Baltimore, Maryland 21218, United States;

<sup>3</sup>State Key Laboratory of Pollution Control and Resources Reuse, College of Environmental Science & Engineering, Tongji University, 1239 Siping Road, Shanghai 200092, China.

\*E-mail: wang\_jianying@tongji.edu.cn (J. Y. Wang), zfchen@tongji.edu.cn (Z. F. Chen)

**Abstract.** Coupling biomass valorization with rechargeable metal-air batteries offers a promising strategy to address energy storage and sustainable synthesis challenges, however, it demands highly active bifunctional catalysts capable of replacing the sluggish oxygen evolution reaction (OER) with value-added biomass electrooxidation. We report here a single-atom nickel-decorated tungsten carbide (Ni-WC<sub>x</sub>) catalyst that



demonstrates exceptional bifunctional activity for both the oxidation of 5-hydroxymethylfurfural (HMF) and the oxygen reduction reaction (ORR). The catalyst achieves near-quantitative conversion of HMF to furandicarboxylic acid (FDCA) with 99% selectivity and shows excellent ORR performance, featuring a half-wave potential ( $E_{1/2}$ ) of 0.855 V. Through *in situ* spectroscopic analysis and multiscale simulations, we reveal a dual role of the atomically dispersed  $\text{Ni}^{\delta+}$  sites: serving as intrinsic active centers and reconstructing the interfacial hydrogen-bond network to facilitate mass transport of bulky HMF molecules. When applied in an HMF-assisted Zn-air battery, the catalyst enables an ultralow charge-discharge voltage gap of 0.71 V at 20  $\text{mA cm}^{-2}$  and remarkable cycling stability. This work proposes a new design strategy for electrocatalysts, emphasizing interfacial solvent engineering as a critical route to advanced hybrid energy-chemical systems.

**Keywords.** Single-atom electrocatalyst; Hybrid zinc-air battery; HMF electrooxidation; Interfacial hydrogen-bond network; Tungsten carbide

## Introduction

The integration of sustainable energy storage with green chemical synthesis represents an important research frontier.<sup>1</sup> A promising strategy to address these dual challenges involves replacing the sluggish oxygen evolution reaction (OER) in rechargeable zinc-air batteries (rZABs) with value-added electrocatalytic reactions, such as the oxidation of biomass-derived platform chemicals.<sup>2</sup> Among these, 5-hydroxymethylfurfural (HMF) is particularly noteworthy. Its conversion to 2,5-



furandicarboxylic acid (FDCA) offers significant appeal, as FDCA serves as a high-value monomer for synthesizing polyethylene furanoate (PEF), a biodegradable alternative to petroleum-based polyethylene terephthalate (PET).<sup>3-5</sup> Coupling the HMF oxidation reaction (HMFOR) with the oxygen reduction reaction (ORR) in a hybrid rZAB system provides dual benefits: reducing the charging overpotential to enhance energy efficiency, while simultaneously enabling sustainable production of valuable chemicals.<sup>6</sup> However, the practical implementation of this technology hinges on the development of highly active, stable, and cost-effective bifunctional electrocatalysts capable of efficiently driving both HMFOR and ORR.<sup>7</sup>

Electrocatalysis is fundamentally governed by interfacial phenomena, involving complex interactions at both solid-state (metal-support) and solid-liquid (catalyst-electrolyte) interfaces.<sup>8, 9</sup> At the solid-state level, constructing a stable and electronically coupled metal-support interface is essential. Single-atom catalysts (SACs) provide exceptional activity due to the unsaturated coordination sites and distinct electronic properties, yet their practical catalytic performance is highly dependent on the choice of support material.<sup>10, 11</sup> While conventional N-doped carbon supports often suffer from insufficient stability due to weak anchoring of single atoms, tungsten carbide ( $WC_x$ ) offers a robust and electronically active alternative. Its Pt-like d-band electronic structure, high electrical conductivity, and replaceable lattice atoms promote efficient charge transfer and strong metal-support interactions, creating an ideal platform for stabilizing single atoms and enhancing their intrinsic activity.<sup>12</sup> Furthermore, dopant-substrate interaction can modulate the electronic structure of  $WC_x$ ,



thereby boosting the intrinsic activity of the substrate.

View Article Online  
DOI: 10.1039/D5SC09133K

Beyond the solid-state interface, interfacial solvent structures play a critical role in diffusion-limited reactions such as HMFOR, where reaction kinetics are strongly influenced by the local electrolyte environment.<sup>13, 14</sup> Although the hydrogen-bond network of water facilitates proton transfer, it can also form a rigid interfacial layer that hinders the diffusion of bulky organic molecules like HMF, a shielding effect that introduces a significant yet often overlooked kinetic barrier.<sup>15</sup> Therefore, reconciling the requirements for optimal performance at both solid-state and solid-liquid interfaces remains a fundamental challenge in catalyst design. A key design principle emerges: engineering atomic-scale solid-state interfaces that can meanwhile modulate the interfacial solvent structure across the electric double layer, thereby alleviating mass transport limitations.

Herein, we report the rational design of a single-atom nickel-decorated tungsten carbide (Ni-WC<sub>x</sub>) catalyst that serves as a high-performance bifunctional electrocatalyst for an advanced rZAB system capable of co-producing FDCA. Distinguished from conventional bifunctional materials, the Ni-WC<sub>x</sub> catalyst features a reaction-selective active site architecture where atomically dispersed Ni<sup>δ+</sup> centers primarily catalyze the HMFOR via a direct Ni<sup>δ+</sup>/Ni<sup>3+</sup> redox cycle, while adjacent electronically modulated W sites serve as the principal centers for the ORR. This site-differentiation strategy effectively minimizes competitive adsorption between HMF and oxygen species, allowing the catalyst to achieve 99% FDCA selectivity at 1.45 V vs. RHE and an impressive ORR half-wave potential ( $E_{1/2}$ ) of 0.855 V that surpasses



commercial Pt/C. Through a combination of *in situ* FTIR spectroscopy, molecular dynamics (MD) simulations, and density functional theory (DFT) calculations, we elucidate a unique promotion mechanism: the Ni<sup>δ+</sup> sites not only provide optimal binding for HMF adsorption but also electrostatically disrupt the rigid interfacial hydrogen-bond network of water, thereby facilitating the mass transfer of bulky organic reactants and OH<sup>-</sup> to the catalytic surface. When deployed as the air cathode in an HMF-assisted rZAB, the catalyst enables an ultra-low charge-discharge voltage gap of 0.71 V at 20 mA cm<sup>-2</sup>, a high power density of 124.7 mW cm<sup>-2</sup>, and excellent long-term stability over 200 hours of continuous operation, all while maintaining uninterrupted FDCA generation. This work establishes a new catalyst design paradigm that highlights the importance of atomic-level control over both the solid-state and solid-liquid interfaces to enhance reaction kinetics and mass transport in advanced electrochemical systems.

## Results and discussion

### Synthesis and Characterization of the Ni-WC<sub>x</sub>

The Ni-WC<sub>x</sub> catalyst was synthesized via a facile sol-gel method followed by pyrolysis. Briefly, dopamine (DA) was employed as a strong chelating agent to uniformly disperse metal atoms within a W-DA-Ni precursor, which was pyrolyzed under nitrogen to yield Ni-WC<sub>x</sub> nanoparticles supported on carbon, as shown in **Fig. 1a**. Scanning electron microscopy (SEM) image shows that Ni-WC<sub>x</sub> exhibits a hierarchical hydrangea-like morphology composed of layered nanosheets assembled



into microspheres (**Fig. 1b**), which facilitates active site exposure and provides ample electrode/electrolyte interface. This morphology remains consistent with that of pristine  $WC_x$  (**Fig. S1**), indicating that Ni incorporation does not alter the overall structure. Transmission electron microscopy (TEM) images confirm that the nanoparticles are firmly embedded in the carbon matrix, as depicted in **Fig. 1c and S2**, and high-resolution TEM (HRTEM) reveals a lattice spacing of 0.251 nm corresponding to the (100) plane of WC (**Fig. 1d**).

Atomic-scale aberration-corrected high-angle annular dark-field scanning transmission electron microscopy (HAADF-STEM) image further reveals isolated Ni atoms incorporated into W-atom arrays (**Fig. 1e**). The intensity contrast, consistent with the atomic numbers of Ni ( $Z = 28$ ) and W ( $Z = 74$ ), along with line-scan profiles (**Fig. 1f**) and 3D atom mapping (**Fig. 1g**), confirms the atomic dispersion of Ni on  $WC_x$ .<sup>16</sup> Energy-dispersive X-ray (EDX) elemental mappings demonstrate homogeneous distribution of Ni, W and C without detectable Ni agglomeration (**Fig. 1h**), collectively verifying the successful synthesis of atomically dispersed Ni on  $WC_x$ .

X-ray diffraction (XRD) patterns of both Ni- $WC_x$  and  $WC_x$  correspond to hexagonal WC (JCPDS No. 01-2755) and  $W_2C$  (JCPDS No. 03-5411) phases, with the (100) plane of WC being predominant (**Fig. 2a**).<sup>17, 18</sup> The absence of Ni-related crystalline phases and the reduced overall crystallinity of Ni- $WC_x$  is consistent with Ni single atoms incorporated into the  $WC_x$  lattice. Raman spectroscopy further supports the conclusion (**Fig. S3**) that the W-C vibration peaks ( $\sim 675$  and  $802\text{ cm}^{-1}$ ) in Ni- $WC_x$  exhibit a red shift compared to pristine  $WC_x$ , indicating an attenuation of W-C bonds





due to Ni doping.

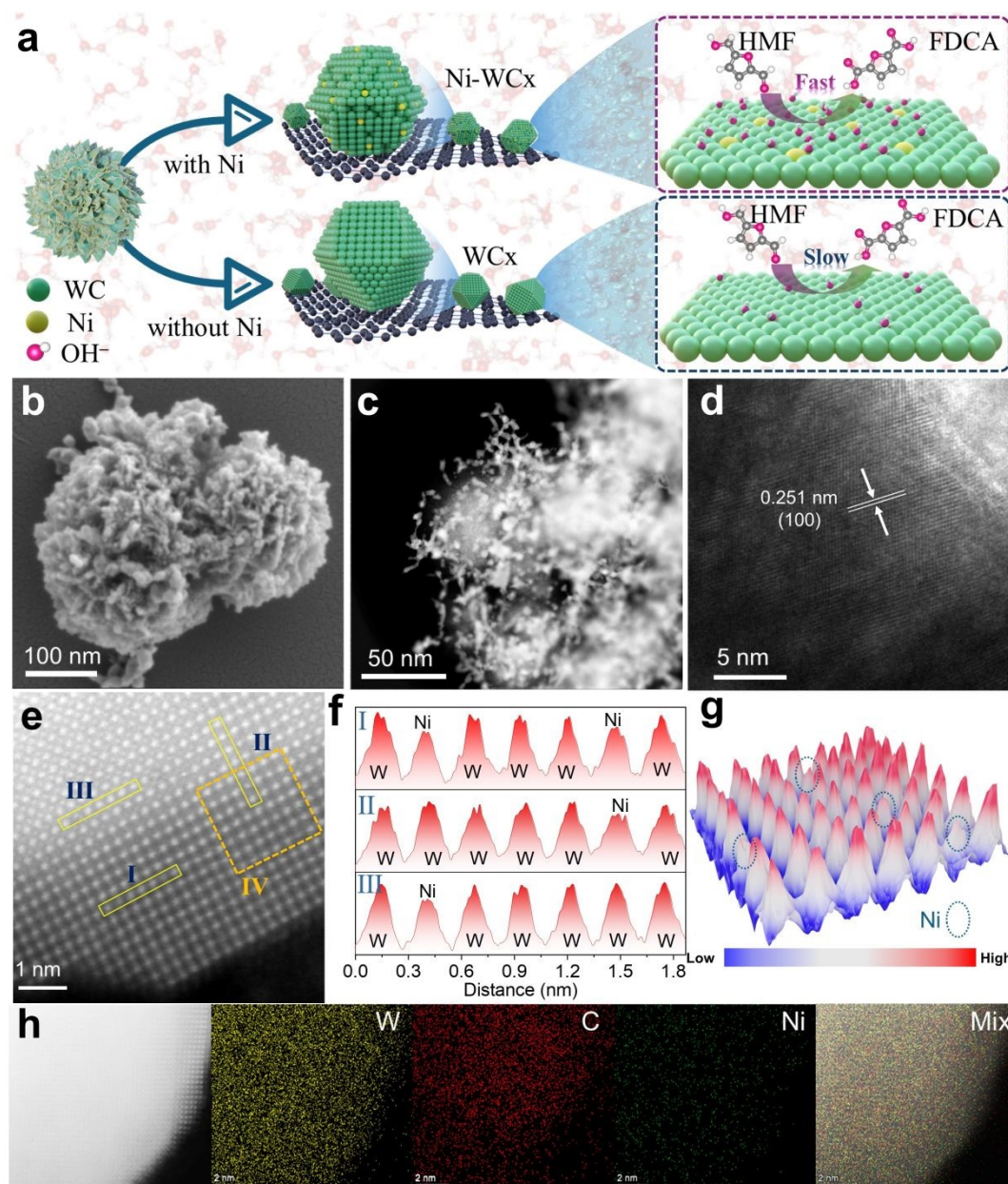


**Figure 1.** Morphological and structural characterization of the synthesized materials. (a) Schematic illustration of Ni-WC<sub>x</sub> and WC<sub>x</sub>, highlighting the atomically engineering effect toward HMFOR. (b) SEM, (c) TEM, and (d) HRTEM images of Ni-WC<sub>x</sub>. (e) HAADF-STEM image of Ni-WC<sub>x</sub>, revealing atomic-scale features. (f) Corresponding intensity profile and (g) 3D atomic-resolution topographic representation derived from IV region in (e). (h) Elemental mapping of W, C and Ni in Ni-WC<sub>x</sub>.





X-ray photoelectron spectroscopy (XPS) was used to analyze the surface electronic states of Ni-WC<sub>x</sub> (survey spectrum in **Fig. S4a**). The high-resolution Ni 2p spectrum (**Fig. 2b**) shows characteristic Ni 2p<sub>3/2</sub> and Ni 2p<sub>1/2</sub> peaks along with satellite features.<sup>19-21</sup> Deconvolution identifies contributions at 853.2 and 868.9 eV, attributed to Ni-C bonding, indicating interaction between Ni atoms and the carbon support.<sup>22</sup> The surface Ni content measured by XPS is 2.25 wt%, aligning closely with the bulk value of 2.33 wt% from inductively coupled plasma-optical emission spectrometry (ICP-OES).

In the W 4f spectrum of Ni-WC<sub>x</sub> (**Fig. 2c**), peaks corresponding to W-C bonds are observed at 31.2 and 33.3 eV, alongside higher binding energy peaks indicative of W<sup>6+</sup> species due to surface oxidation.<sup>23, 24</sup> Notably, the W 4f peaks exhibit a positive shift compared to pristine WC<sub>x</sub>, implying reduced electron density around W atoms due to electron transfer from the WC<sub>x</sub> support to Ni. This electronic interaction highlights the role of Ni doping in modulating the catalyst's interfacial properties. Further support comes from the C 1s spectrum (**Fig. S4b**), which displays fitted peaks for C-W/Ni (283.0 eV), C-C (284.1 eV), and C-O (285.3 eV).<sup>22</sup>



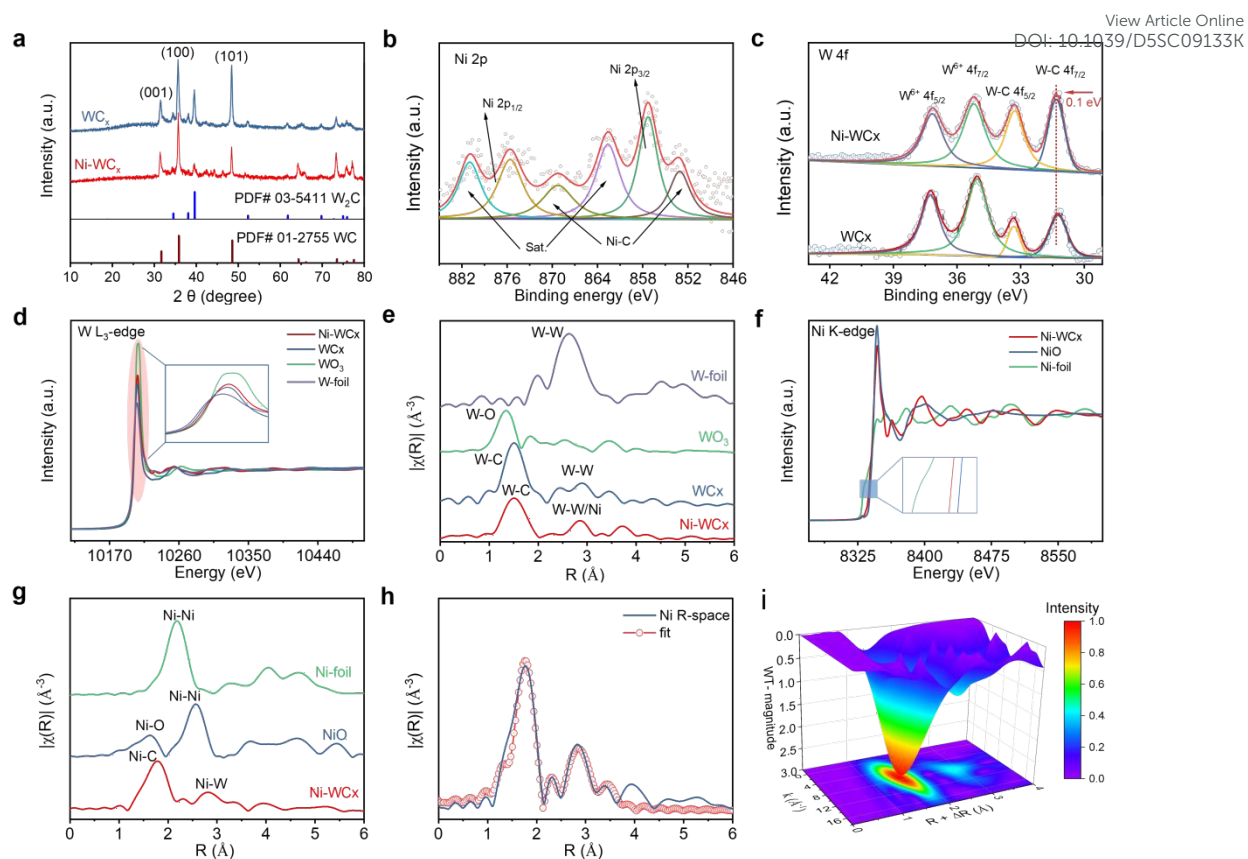


**Figure 2.** Structural characterization. (a) XRD patterns of Ni-WC<sub>x</sub> and WC<sub>x</sub>. High-resolution XPS spectra of (b) Ni 2p for Ni-WC<sub>x</sub> and (c) W 4f for both Ni-WC<sub>x</sub> and WC<sub>x</sub>. (d) Normalized XANES, and (e) FT-EXAFS spectra at the W L<sub>3</sub>-edge. (f) Normalized XANES and (g) FT-EXAFS spectra at the Ni K-edge. (h) Corresponding fitting curves for the FT-EXAFS spectrum at the Ni K-edge for Ni-WC<sub>x</sub>, presented in R space. (i) Wavelet transform analysis of the EXAFS spectrum at the Ni K-edge for Ni-WC<sub>x</sub>.

Synchrotron-based X-ray absorption fine structure (XAFS) analysis was conducted to probe the local coordination and electronic states of W and Ni in Ni-WC<sub>x</sub>. At the W L<sub>3</sub>-edge, the XANES spectrum of Ni-WC<sub>x</sub> (**Fig. 2d**) displays enhanced white-line intensity relative to WC<sub>x</sub>, consistent with XPS results and indicative of an increased



oxidation state of W due to Ni doping.<sup>25</sup> FT-EXAFS analysis reveals that Ni-WC<sub>x</sub> maintains a primary W-C coordination shell similar to WC<sub>x</sub>, though with slightly increased coordination numbers in both W-C and W-W/Ni paths (**Fig. 2e, S5 and Table S1**).

For the Ni K-edge, the XANES spectrum (**Fig. 2f**) confirms the presence of oxidized Ni<sup>δ+</sup> species, with an average valence state of approximately + 1.52 derived from linear combination fitting (**Fig. S6**), in agreement with charge transfer from W to Ni as inferred from XPS and W L<sub>3</sub>-edge data.<sup>26, 27</sup> The FT-EXAFS spectrum at the Ni K-edge (**Fig. 2g**) exhibits a main peak at 1.80 Å assigned to Ni-C coordination, and a distinct secondary peak at 2.84 Å corresponding to Ni-W scattering. The absence of Ni-Ni paths and the presence of Ni-W bonding provide direct evidence for atomic dispersion and substitutional doping of Ni into W sites. This conclusion is further supported by wavelet transform (WT) analysis (**Fig. 2i**). Quantitative EXAFS fitting (**Fig. 2h, S7 and Table S1**) yields a Ni-C coordination number of 3.5, comparable to the W-C coordination number (3.8) in WC<sub>x</sub>, corroborating the substitutional doping model. Together, these results unequivocally confirm the successful incorporation of atomically dispersed Ni<sup>δ+</sup> into the WC<sub>x</sub> framework.

### Performance of electrocatalytic oxidation of HMF

The electrocatalytic HMFOR performance of Ni-WC<sub>x</sub> was assessed in a three-electrode system with 1.0 M KOH. As shown by the linear sweep voltammetry (LSV) curves in **Fig. 3a**, without HMF, the catalyst exhibits only a minor pre-wave at 1.36 V vs. RHE prior to the onset of OER, which is associated with oxidation of Ni species.<sup>28</sup>



Upon adding 20 mM HMF, a substantial current increase occurs following Ni oxidation.

The potential required to reach  $10 \text{ mA cm}^{-2}$  is significantly lower for HMFOR (1.39 V) than for OER (1.56 V). The Tafel slope for HMFOR ( $35.7 \text{ mV dec}^{-1}$ ) is also much smaller than that for OER ( $57.4 \text{ mV dec}^{-1}$ ) (**Fig. 3b**), and the enhanced kinetics of HMFOR are further supported by electrochemical impedance spectroscopy (EIS) (**Fig. S8**). In stark contrast, both the  $\text{WC}_x$  and the commercial  $\text{IrO}_2$  benchmark exhibit negligible current responses above OER background in the HMF-containing electrolyte (**Fig. 3c and S9**). By normalizing to the electrochemically active surface area (ECSA), Ni- $\text{WC}_x$  maintained the highest current density compared to the counterparts, confirming the superior intrinsic activity of Ni- $\text{WC}_x$  (**Fig. S10 and S11**). This result underscores the essential role of the atomically dispersed  $\text{Ni}^{\delta+}$  sites toward HMFOR. Based on the linear current-concentration relationship (**Fig. S12**), 20 mM HMF was selected for all further tests to balance reactivity and selectivity.

Potentiostatic electrolysis at 1.45 V vs. RHE was used to evaluate product selectivity and Faradaic efficiency (FE) (**Fig. S13-S15**). High-performance liquid chromatography (HPLC) analysis (**Fig. 3d-e**) shows continuous consumption of HMF and accumulation of FDCA, accompanied by a visible color change from yellow to colorless. Ni- $\text{WC}_x$  achieves 99.20% HMF conversion, 98.98% FDCA selectivity, and a FE of 97.37% (**Fig. S16**). The oxidation of HMF to FDCA follows two possible pathways (**Fig. 3f**): Pathway I begins with oxidation of the aldehyde group to form 5-hydroxymethyl-2-furancarboxylic acid (HMFA), while Pathway II starts with hydroxyl group oxidation to yield 2,5-diformylfuran (DFF).<sup>29</sup> Both routes converge via



formyl-2-furancarboxylic acid (FFCA) before final oxidation to FDCA. HPLC analysis during electrolysis detected HMFCa and FFCA, but nearly no DFF, indicating that HMFOR over the Ni-WC<sub>x</sub> catalyst occurs predominantly through Pathway I: HMF → HMFCa → FFCA → FDCA. Recycling tests demonstrate excellent stability over six cycles with no significant activity loss (**Fig. 3g and S17**). Post-test characterization (TEM, XRD, XPS; **Fig. S18 – S20**) results confirm no observable changes in morphology, structure, or chemical state, affirming the robust stability of Ni-WC<sub>x</sub>.

To further elucidate the reaction mechanism, *in situ* Fourier transform infrared (FTIR) spectroscopy was used to track real-time species evolution during HMFOR.<sup>30</sup> The results showed new characteristic peaks emerging at 1.36 V vs. RHE (**Fig. 3h**), consistent with the EIS results. With increasing potential (1.40 – 1.60 V), product-related peaks intensify, while HMF peaks (1655 and 1519 cm<sup>-1</sup>) continuously decreased. Peaks corresponding to HMFCa (1596, 1525 cm<sup>-1</sup>), FFCA (1407, 1276 cm<sup>-1</sup>), and FDCA (1353, 1214 cm<sup>-1</sup>) were clearly observed, whereas no DFF intermediate was detected.<sup>31, 32</sup> These results confirm further that HMFOR follows Pathway I (HMF → HMFCa → FFCA → FDCA). A slight HMF consumption observed below 1.32 V may be attributed to a minor side reaction such as the Cannizzaro reaction prior to electro-oxidation.<sup>33</sup>

Multi-potential step chronoamperometry was employed to identify the active species as shown in **Fig. S21**. In the absence of HMF, a reduction peak appears at 1.1 V, corresponding to the reduction of electrogenerated Ni<sup>3+</sup> species. This peak disappears entirely when HMF is present, indicating that Ni<sup>3+</sup> is chemically consumed



by HMF rather than electrochemically reduced.<sup>34</sup> This result provides strong evidence that the  $\text{Ni}^{\delta+}/\text{Ni}^{3+}$  redox couple acts as the catalytic center for HMF oxidation.

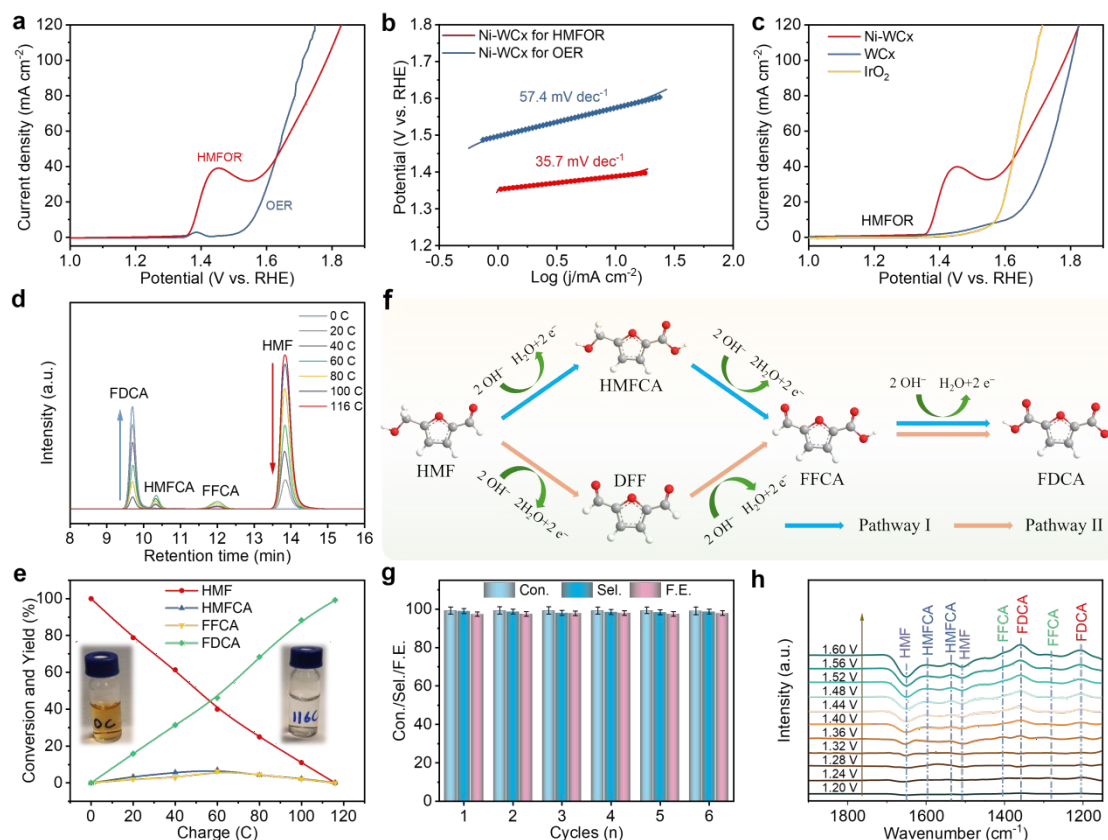


**Figure 3.** Electrocatalytic HMFOR performance evaluations. (a) LSV curves of Ni-WC<sub>x</sub> in 1 M KOH with and without 20 mM HMF, and (b) corresponding Tafel plots. (c) LSV curves illustrating the HMFOR performance of Ni-WC<sub>x</sub>, WC<sub>x</sub> and IrO<sub>2</sub>. (d) HPLC curves with increasing charge accumulation at 1.45 V vs. RHE. (e) Charge-dependent concentration for HMF, FDCA, HMFCA, and FFCA. (f) Two principal reaction pathways for oxidation of HMF to FDCA. (g) Conversion, selectivity and Faradaic efficiency for FDCA production over six sequential electrolysis cycles. (h) *In situ* FTIR spectra of Ni-WC<sub>x</sub> obtained at various applied potentials during HMFOR.





The introduction of  $\text{Ni}^{\delta+}$  sites is proposed to serve not only as intrinsic active centers but also to modulate the catalyst-electrolyte interface by restructuring interfacial water, thereby influencing the adsorption and transfer of  $\text{OH}^-$  and organic substrates during HMFOR.<sup>35</sup> To validate this, systematic interfacial studies were conducted. Zeta potential measurements in 1.0 M KOH showed that  $\text{Ni-WC}_x$  (− 25.4 mV) possesses a more negative surface charge than  $\text{WC}_x$  (− 17.8 mV), signifying more  $\text{OH}^-$  in the inner Helmholtz plane (**Fig. 4a**).<sup>13</sup> This  $\text{OH}^-$ -enriched interface is a direct consequence of the  $\text{Ni}^{\delta+}$  sites perturbing the local solvent environment and reorganizing the hydrogen bond network.<sup>36</sup> Cyclic voltammetry (CV) curves between 0.7 – 1.0 V (**Fig. 4b and S22**) showed a pronounced \*OH adsorption peak at lower potential on  $\text{Ni-WC}_x$  than on  $\text{WC}_x$ .<sup>37</sup> This peak decreased upon the introduction of HMF, whereas the corresponding signal on  $\text{WC}_x$  remained almost unchanged. Notably, the peak current of  $\text{Ni-WC}_x$  remained significantly higher than that of  $\text{WC}_x$ , both with and without HMF, indicating a strong co-adsorption affinity for both  $\text{OH}^-$  and HMF, a crucial feature for efficient HMFOR.<sup>38</sup>

To directly probe the reorganization of the hydrogen-bond network, potential-dependent *in situ* FTIR spectroscopy was applied to the O-H stretching region ( $\nu(\text{O-H})$ ). For the  $\text{Ni-WC}_x$  electrode (**Fig. 4c**), a clear potential-dependent blueshift occurred in the  $\nu(\text{O-H})$  bands, particularly for those of non-hydrogen-bonded water molecules, indicating a weakened interfacial hydrogen-bond network due to electrostatic effects from accumulated  $\text{OH}^-$  near  $\text{Ni}^{\delta+}$  sites.<sup>39</sup> In contrast, the  $\nu(\text{O-H})$  band for  $\text{WC}_x$  remained stable across potentials (**Fig. 4d**), suggesting a rigid hydrogen-bond network that



impedes  $\text{OH}^-$  adsorption and transport. These results demonstrate that  $\text{Ni}^{\delta+}$  incorporation fundamentally alters interfacial water dynamics, forming an electrostatically modulated environment that enhances mass transfer and promotes HMFOR kinetics.

To elucidate how  $\text{Ni}^{\delta+}$  sites reorganize interfacial water at the molecular level, molecular dynamics (MD) simulations were carried out. MD snapshots and concentration profiles of oxygen atoms in water normal to the surface (**Fig. 4e-g**) show that  $\text{Ni}^{\delta+}$  strengthens electrostatic catalyst-water interactions, drawing water closer to the surface.<sup>35</sup> Analysis of the hydrogen-bond (H-bond) network versus distance from the surface (**Fig. 4h**) reveals that  $\text{Ni-WC}_x$  has fewer H-bonds and a longer average bond length (3.042 Å) in the first water layer ( $\sim 3$  Å) compared to  $\text{WC}_x$  (3.032 Å), whereas the second layer ( $\sim 4.5$  Å) shows higher H-bond density. Further analysis of the MD trajectories reveals that the lateral diffusion coefficient of interfacial HMF, extracted from the mean-squared displacement parallel to the surface (**Fig. S23**), is significantly larger on  $\text{Ni-WC}_x$  than on  $\text{WC}_x$ . Additionally, angular distribution analysis (**Fig. S24**) shows that HMF on  $\text{Ni-WC}_x$  adopts a preferred "lying-down" orientation, which brings the reactive aldehyde group into close proximity with the active sites and facilitates surface interaction, whereas it exhibits a random orientation on  $\text{WC}_x$ . These results indicate that  $\text{Ni}^{\delta+}$  induces a targeted reconstruction of the interfacial H-bond network, rather than inducing a broad destabilization.<sup>40</sup> The disrupted first layer forms a dynamic, loose microenvironment that reduces mass transfer resistance for bulky HMF molecules and facilitates  $\text{OH}^-$  shuttling.



To elucidate the origin of the enhanced HMFOR activity, systematic DFT calculations were conducted. Charge density difference plots (**Fig. 4i**) reveal significant interfacial charge redistribution in Ni-WC<sub>x</sub>, with electron accumulation between Ni and the WC<sub>x</sub> support, confirming strong electronic coupling. Correspondingly, the total density of states (TDOS) near the Fermi level is higher in Ni-WC<sub>x</sub> than in WC<sub>x</sub> (**Fig. 4j**), indicating improved charge transfer. Projected density of states (PDOS) analysis (**Fig. S25**) further shows that Ni<sup>δ+</sup> induces delocalization of electrons in adjacent W 5d orbitals.<sup>41</sup> This electronic modulation reshapes the surface electrostatic environment, strengthening interactions with interfacial water and providing a fundamental rationale for the restructured hydrogen-bond network observed in MD and FTIR. The optimized electronic structure of Ni-WC<sub>x</sub> leads to superior reaction kinetics. HMF adsorbs more strongly on the Ni site (− 0.246 eV) than on WC<sub>x</sub> (− 0.112 eV), with the aldehyde group tilting toward Ni in an ideal configuration for C-H activation (**Fig. S26**).<sup>42</sup> Free energy calculations along Pathway I (**Fig. 4k and S27**) identify FFCA\* dehydrogenation as the rate-determining step (RDS). Ni doping drastically reduces this barrier from 0.776 eV (WC<sub>x</sub>) to 0.569 eV (Ni-WC<sub>x</sub>). These results demonstrate that synergistic electronic coupling between Ni<sup>δ+</sup> and WC<sub>x</sub> enhances intermediate adsorption and reduces the RDS energy barrier, thereby significantly improving intrinsic HMFOR activity.



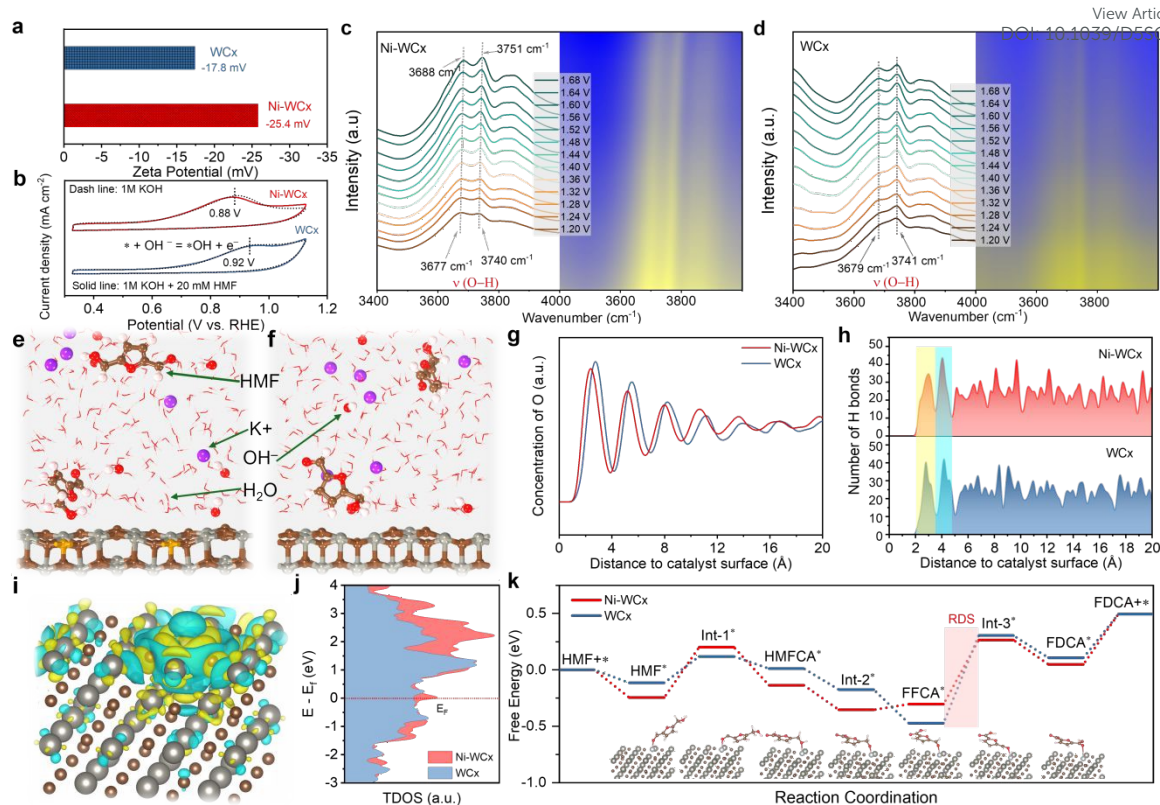


**Figure 4.** Mechanism investigation of catalyst-electrolyte interface in HMFOR. (a) Zeta potential of Ni-WCx and WCx in 1 M KOH. (b) CV curves of Ni-WCx and WCx in KOH with and without 20 mM HMF. *In situ* FTIR spectra highlighting the non-hydrogen bonded O-H stretching vibration mode acquired within 1.20 – 1.60 V for (c) Ni-WCx and (d) WCx in 1 M KOH, accompanied by corresponding 2D visualizations. MD simulated representative snapshots of electrode-electrolyte interface for (e) Ni-WCx and (f) WCx, with Ni, W and C atoms represented by yellow, gray and brown spheres, respectively. (g) Spatially resolved concentration profiles of oxygen atoms in water, plotted as a function of distance normal to the Ni-WCx and WCx surfaces. (h) Statistical distributions of hydrogen bond counts as a function of distance normal to the Ni-WCx and WCx surfaces. (i) Differential charge density map of Ni-WCx, indicating regions of charge accumulation (yellow) and depletion (blue). (j) TDOS for Ni-WCx



and WC<sub>x</sub>. (k) Free energy diagrams for the HMFOR pathway on Ni-WC<sub>x</sub> and WC<sub>x</sub>. View Article Online  
DOI: 10.1039/D5SC09133K

### Performance of oxygen reduction reaction

The ORR performance of Ni-WC<sub>x</sub> was systematically assessed in O<sub>2</sub>-saturated 0.1 M KOH using the rotating disk electrode (RDE) method, with WC<sub>x</sub> and commercial Pt/C as benchmarks. Preliminary CV curves confirm intrinsic ORR activity for both Ni-WC<sub>x</sub> and WC<sub>x</sub> (**Fig. S28**). LSV curves in **Fig. 5a** show that Ni-WC<sub>x</sub> exhibits a higher half-wave potential ( $E_{1/2} = 0.855$  V) and larger limiting current density ( $J_L = 6.16$  mA cm<sup>-2</sup>) than both WC<sub>x</sub> ( $E_{1/2} = 0.747$  V,  $J_L = 4.98$  mA cm<sup>-2</sup>) and Pt/C ( $E_{1/2} = 0.850$  V,  $J_L = 5.89$  mA cm<sup>-2</sup>). The Tafel slope of Ni-WC<sub>x</sub> (39.1 mV dec<sup>-1</sup>) is also significantly lower than those of WC<sub>x</sub> (64.9 mV dec<sup>-1</sup>) and Pt/C (63.6 mV dec<sup>-1</sup>), indicating faster reaction kinetics, as illustrate in **Fig. 5b**. This superior catalytic activity is further supported by its superior kinetic current density ( $J_k$ , **Fig. 5c**) and ECSA-normalized current density (**Fig. S29**). To elucidate the ORR pathway, the number of electrons transferred ( $n$ ) was determined via rotating ring-disk electrode (RRDE) measurements and Koutecky-Levich (K-L) analysis. RRDE results (**Fig. 5d**) show an  $n$  value of 3.9 and a low H<sub>2</sub>O<sub>2</sub> yield (< 8%), consistent with the 4e<sup>-</sup> pathway. K-L plots from LSVs at multiple rotation speeds also confirm  $n \approx 4.0$  (**Fig. S30**), reinforcing the dominant 4e<sup>-</sup> reduction mechanism.



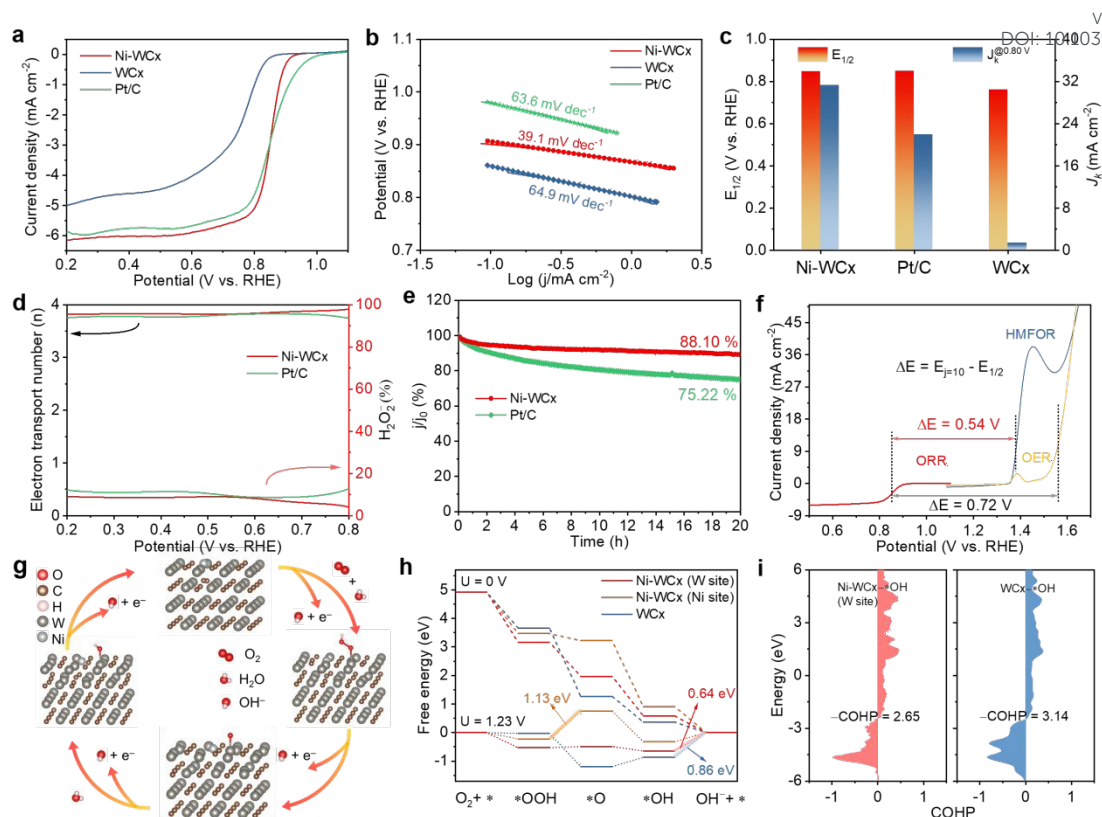


**Figure 5.** Electrocatalytic ORR performance. (a) ORR polarization curves in O<sub>2</sub>-saturated 0.1 M KOH at a rotating rate of 1600 rpm, (b) Tafel plots, and (c) analysis of E<sub>1/2</sub> and J<sub>k</sub> at 0.80 V of Ni-WC<sub>x</sub>, WC<sub>x</sub> and Pt/C. (d) Determination of electron transfer numbers and H<sub>2</sub>O<sub>2</sub> yield during the ORR process. (e) Chronoamperometry stability assessment conducted at 0.40 V vs. RHE. (f) Overall polarization curves of Ni-WC<sub>x</sub> toward the ORR and OER/HMFOR. (g) Proposed mechanism elucidating ORR on Ni-WC<sub>x</sub>. (h) Free energy diagram of ORR on Ni-WC<sub>x</sub> and WC<sub>x</sub>. (i) COHP analysis and the corresponding ICOHP values quantifying the bonding interaction between adsorbed \*OH and Ni-WC<sub>x</sub> and WC<sub>x</sub> surfaces.

The long-term durability of Ni-WC<sub>x</sub> was assessed via chronoamperometry measurement. As can be seen (**Fig. 5e**), Ni-WC<sub>x</sub> retained 88.1% of its initial current after 20 hours, significantly outperforming Pt/C (75.2%). Post-test ORR polarization





curves (**Fig. S31**) show that the change of  $E_{1/2}$ , onset potential and  $J_L$  of Ni-WC<sub>x</sub> was insignificant, indicating little loss of intrinsic activity. TEM image (**Fig. S32**) reveals that the hydrangea-like microspheres and nanosheet subunits were preserved without noticeable aggregation or collapse. XRD pattern after ORR (**Fig. S33**) retained the characteristic WC/W<sub>2</sub>C reflections without phase change, while XPS analysis (Ni 2p and W 4f; **Fig. S34**) confirms that Ni remained in an oxidized Ni<sup>δ+</sup> state and the W–C framework was largely maintained. These results collectively demonstrate the robust chemical and structural stability of Ni-WC<sub>x</sub> under harsh oxidative conditions.

The bifunctional performance was quantified using the potential gap  $\Delta E$ , defined as  $\Delta E = E_{j=10}(\text{OER/HMFOR}) - E_{1/2}(\text{ORR})$ .<sup>43</sup> A smaller  $\Delta E$  indicates better catalytic reversibility. Ni-WC<sub>x</sub> achieves an exceptionally low  $\Delta E$  of 0.54 V for the ORR||HMFOR couple, considerably lower than 0.72 V for ORR||OER on the same catalyst (**Fig. 5f**). This result underscores the kinetic advantage of replacing OER with HMFOR. Moreover, this performance surpasses most recently reported non-noble metal catalysts (**Table S2**).

To definitively ascertain the active site identity for ORR, selective site-blocking investigations were conducted utilizing thiocyanate (SCN<sup>−</sup>), a strong blocking agent for Ni sites. As shown in **Fig. S35**, the cathodic current observed on the Ni-WC<sub>x</sub> electrode remained largely unperturbed following the introduction of 10 mM KSCN into the O<sub>2</sub>-saturated 0.1 M KOH electrolyte, indicating a substantial resistance to selective poisoning. Specifically, this limited effect suggests that Ni<sup>δ+</sup> sites are not the primary



active centers for the ORR, or at least that their blockage does not suppress the main reaction pathway.

To elucidate the ORR mechanism on Ni-WC<sub>x</sub> at the atomic level, DFT calculations were performed to evaluate the thermodynamics of key intermediates (\*OOH, \*O, \*OH) on different active sites of W and Ni sites on Ni-WC<sub>x</sub>, as well as W site on pristine WC<sub>x</sub> (**Fig. 5g and S36**).<sup>44</sup> The free energy diagrams at U = 0 V show a downhill trend for all sites (**Fig. 5h**). At the equilibrium potential (U = 1.23 V), the RDS on the Ni site is \*OOH dissociation to \*O, with a high energy barrier of 1.13 eV. In contrast, the RDS on W sites (both in Ni-WC<sub>x</sub> and WC<sub>x</sub>) is \*OH desorption. Notably, the energy barrier for this step is significantly lower on the W site of Ni-WC<sub>x</sub> (0.64 eV) than on pristine WC<sub>x</sub> (0.86 eV), identifying W atoms near Ni as the primary ORR active sites and highlighting the promotional role of Ni doping.

To understand the electronic origin of the reduced barrier, the Crystal Orbital Hamilton Population (COHP) analysis was conducted to probe the bonding strength of the key \*OH intermediate.<sup>45</sup> The integrated COHP (ICOHP) value for the W-OH bond on Ni-WC<sub>x</sub> is |−2.65|, smaller than that on WC<sub>x</sub> (|−3.14|), indicating a weaker W-OH interaction that facilitates \*OH removal (**Fig. 5i and S37**). These results confirm that Ni doping electronically modulates adjacent W sites, optimizing the adsorption/desorption of oxygen intermediates and enhancing intrinsic ORR activity, consistent with experimental observations.

It is noteworthy that Ni-WC<sub>x</sub> catalyst exhibits reaction-selective active sites, a critical design feature that enables its exceptional bifunctional performance. Different



from conventional bifunctional catalysts where the same active site mediates both reactions, Ni-WC<sub>x</sub> leverages a synergistic dual-site mechanism: atomically dispersed Ni<sup>δ+</sup> centers catalyze HMFOR through direct participation in the Ni<sup>δ+</sup>/Ni<sup>3+</sup> redox cycle, while adjacent W sites, electronically modulated by Ni incorporation, serve as the primary ORR active centers with optimized oxygen intermediate binding. This site-differentiation strategy not only maximizes the intrinsic activities of both reactions but also minimizes potential competitive adsorption between HMF and O<sub>2</sub>-derived species, contributing to the superior performance in HMF-assisted Zn-air batteries.

### Performance of HMF-assisted rechargeable Zn-Air redox battery

Utilizing the outstanding bifunctional activity of Ni-WC<sub>x</sub>, an HMF-assisted rechargeable rZAB was constructed to assess its practical performance (**Fig. 6a**). Substituting the OER with HMFOR offers multiple key benefits: it enables the coproduction of valuable chemicals, lowers the charging voltage to mitigate cathode degradation from high overpotentials,<sup>46, 47</sup> and eliminates O<sub>2</sub> bubble formation, thereby enhancing interfacial stability, particularly at high current densities<sup>48, 49</sup>.

For comparison, conventional rZABs with Ni-WC<sub>x</sub> or Pt/C-IrO<sub>2</sub> as a cathode for ORR/OER were also assembled. The HMF-assisted battery achieved an open-circuit voltage (OCV) of 1.483 V, comparable to the ORR/OER Ni-WC<sub>x</sub> battery (1.485 V) and higher than the ORR/OER Pt/C-IrO<sub>2</sub> battery (1.457 V, **Fig. 6b and S38**). Charge-discharge polarization curves showed that the HMF-assisted system maintains a smaller voltage gap than that using a Pt/C-IrO<sub>2</sub> cathode across current densities from 1 to 75



$\text{mA cm}^{-2}$  (**Fig. S39**), indicating improved energy efficiency. The gap increases at higher currents due to competing OER.

The HMF-assisted rZAB reached a peak power density of  $124.7 \text{ mW cm}^{-2}$  (**Fig. 6c**), on par with the ORR/OER Ni-WC<sub>x</sub> battery and superior to the ORR/OER Pt/C-IrO<sub>2</sub> battery (**Fig. S40**), confirming that HMF addition does not hinder discharge performance. It delivered a high specific capacity of  $749.85 \text{ mA h g}^{-1}$  at  $20 \text{ mA cm}^{-2}$ , exceeding the ORR/OER Pt/C-IrO<sub>2</sub> battery ( $720.02 \text{ mA h g}^{-1}$ , **Fig. S41**). The HMF-assisted rZAB also exhibited excellent rate capability with stable discharge plateaus from 1 to  $50 \text{ mA cm}^{-2}$  and rapid potential recovery after high-current pulses (**Fig. 6d**). Constant-current charging confirmed consistently lower charging voltages for the HMF-assisted system across all currents (**Fig. 6e and S42**), demonstrating that HMFOR effectively reduces charging overpotential and improves energy efficiency.

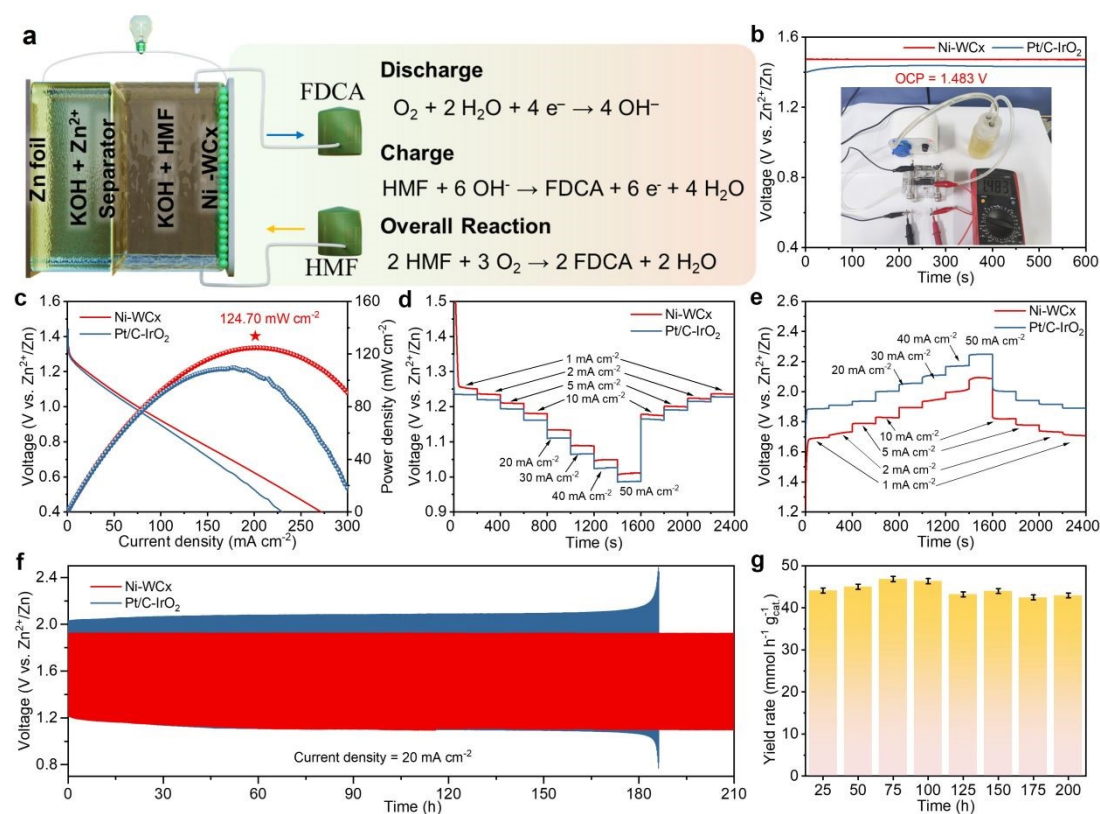


**Figure 6.** Rechargeable Zn-air battery performances evaluations. (a) Schematic illustration of HMF-assisted flow-type rZAB. (b) Open-circuit voltages. (c) Discharge polarization curves and corresponding power density profiles for the rZAB. (d) Galvanostatic discharge and (e) galvanostatic charge curves under different current densities. (f) Long-term cycling stability assessed via galvanostatic discharge-charge measurements at a current density of  $20 \text{ mA cm}^{-2}$ , and (g) the associated yield rate of FDCA.

To evaluate the viability of the HMF-assisted battery as a dual-output system, its long-term cycling performance was tested at  $20 \text{ mA cm}^{-2}$ . The HMF-assisted rZAB exhibited a significantly smaller initial voltage gap (charge: 1.925 V, discharge: 1.214 V) than the ORR/OER Pt/C-IrO<sub>2</sub> battery (2.031 V, 1.234 V), achieving a high initial round-trip efficiency of 63.1% (**Fig. 6f**). After 200 hours of cycling, it maintained excellent stability with minimal voltage decay and a round-trip efficiency of 56.4%. In contrast, the ORR/OER Pt/C-IrO<sub>2</sub> battery showed severe polarization and failed after ~180 hours, highlighting the superior durability and energy efficiency of the HMF-assisted system.

Simultaneously, the battery continuously produced FDCA at a high rate exceeding  $42.50 \text{ mmol h}^{-1} \text{ g}_{\text{cat}}^{-1}$  throughout the 200-hour test (**Fig. 6g**). This dual functionality, which combining stable energy storage with efficient chemical production, outperforms most previously reported hybrid rZAB systems (**Table S3**). Furthermore, a single HMF-assisted rZAB successfully powered an electronic timer for over 24 hours (**Fig. S43**), demonstrating practical applicability. These results thus establish the HMF-



assisted rZAB as a highly efficient and durable bifunctional system that integrates energy storage with sustainable chemical synthesis.

## Conclusions

In summary, we have successfully developed a single-atom Ni-decorated tungsten carbide catalyst with exceptional bifunctional activity for both HMF oxidation and oxygen reduction. When deployed in a hybrid zinc-air battery, this catalyst enables a system that simultaneously achieves a low charge-discharge voltage gap, outstanding cycling stability, and continuous production of FDCA with high selectivity and Faradaic efficiency.

Beyond its catalytic performance, this work reveals a synergistic mechanism that transcends conventional active-site design. We demonstrate that atomically dispersed  $\text{Ni}^{\delta+}$  sites serve not only as intrinsic active centers but also as atomic-level modulators of the catalyst-electrolyte interface. Through integrated experiments and multiscale simulations, we show that  $\text{Ni}^{\delta+}$  incorporation reconstructs the interfacial water structure, disrupting rigid hydrogen-bond networks and alleviating mass transport limitations for bulky organic molecules. By highlighting the critical role of interfacial solvent engineering alongside electronic structure optimization, this study establishes a new design paradigm for multifunctional electrocatalysts, opening avenues for integrated energy conversion and sustainable chemical synthesis.

## Author contributions





Xiaoyang He: conceptualization, data curation, formal analysis, investigation, methodology, software, writing – original draft, and writing – review & editing; Dengke Xiong, Kaiyan Zhang, Wei Wang, Shujie Xue: methodology, data curation, formal analysis, investigation, and software; Jianying Wang, Deli Wu: conceptualization, resources, supervision; Zuofeng Chen: conceptualization, formal analysis, investigation, methodology, resources, funding acquisition, supervision, project administration, and writing – review & editing.

### Conflicts of interest

There are no conflicts of interest to declare

### Data availability

The data supporting this article have been included as part of the Supplementary Information. Supplementary information: Details of experimental section including chemical and materials; material characterizations; product separation and analysis; *in situ* FTIR; DFT calculation and MD methods; additional morphological; structural and compositional characterizations of Ni-WC<sub>x</sub> and contrast samples; stability characterizations; standard curves of product analysis, calculated Faradaic efficiencies; supplementary figures and tables and optical photograph of the HMF-assisted Zn-air battery. See DOI:

### Acknowledgements

This work was supported by the National Key R&D Program of China (2024YFA1211004), the National Natural Science Foundation of China (22402150),



the Natural Science Foundation of Shanghai Municipality (23ZR1464800, 24ZR1470200), the Fundamental Research Funds for the Central Universities (22120240296).

## References

1. G. Li, R. Wang, J. Pang, A. Wang, N. Li and T. Zhang, *Chem. Rev.*, 2024, **124**, 2889-2954.
2. X. Liu, X. He, D. Xiong, G. Wang, Z. Tu, D. Wu, J. Wang, J. Gu and Z. Chen, *ACS Catal.*, 2024, **14**, 5366-5376.
3. L. Guo, X. Zhang, L. Gan, L. Pan, C. Shi, Z. F. Huang, X. Zhang and J. J. Zou, *Adv. Sci.*, 2023, **10**, e2205540.
4. D. Chen, Y. Ding, X. Cao, L. Wang, H. Lee, G. Lin, W. Li, G. Ding and L. Sun, *Angew. Chem. Int. Ed.*, 2023, **62**, e202309478.
5. Z. Li, L. Sun, Y. Zhang, Y. Han, W. Zhuang, L. Tian and W. Tan, *Coord. Chem. Rev.*, 2024, **510**, 215837.
6. M. Wu, Y. Xu, J. Luo, S. Yang, G. Zhang, L. Du, H. Luo, X. Cui, Y. Yang and S. Sun, *Angew. Chem. Int. Ed.*, 2024, **63**, e202410845.
7. Y. Wang, S. Lu, M. Yang, Z. Zhang and J. Zhang, *Mater. Today Sustain.*, 2024, **25**, 100630.
8. Y. Lin, B. Chen, D. Huang, Z. Yang, A. Lu, Z. Shi, Y. Liu, J. Fang, H. Li and T. Zhai, *Angew. Chem. Int. Ed.*, 2025, **64**, e202502151.
9. R. Zhao, Q. Wang, Y. Yao, R. Wang, L. Zhao, Z. Hu, C.-W. Kao, T.-S. Chan,



- W. Li, Q. Zheng, J. Wang, X. Zou, K. Wang, J. Dai, X.-K. Gu and L. Zhang, *Sci. Adv.*, 2025, **11**, eadul602.
10. Y. Li, Y. Li, H. Sun, L. Gao, X. Jin, Y. Li, Z. Lv, L. Xu, W. Liu and X. Sun, *Nano-Micro Lett.*, 2024, **16**, 139.
  11. Z. Li, W. Na, C. Tian, J. Dong, L. Tian, M. Ma, T. Li and Y. Zhang, *Chem. Eng. J.*, 2025, **526**, 171146.
  12. Y. Liu, T. G. Kelly, J. G. Chen and W. E. Mustain, *ACS Catal.*, 2013, **3**, 1184-1194.
  13. P. Zhou, X. Lv, S. Tao, J. Wu, H. Wang, X. Wei, T. Wang, B. Zhou, Y. Lu, T. Frauenheim, X. Fu, S. Wang and Y. Zou, *Adv. Mater.*, 2022, **34**, 2204089.
  14. D. Xiao, X. Bao, D. Dai, Y. Gao, S. Si, Z. Wang, Y. Liu, P. Wang, Z. Zheng, H. Cheng, Y. Dai and B. Huang, *Adv. Mater.*, 2023, **35**, 2304133.
  15. Z. Yang, L. Chen, Y. Yin, C. Wei, Z. Xue and T. Mu, *Energ. Environ. Sci.*, 2024, **17**, 8801-8809.
  16. S. Li, B. Chen, Y. Wang, M.-Y. Ye, P. A. van Aken, C. Cheng and A. Thomas, *Nat. Mater.*, 2021, **20**, 1240-1247.
  17. L. Wang, Z. Xu, C.-H. Kuo, J. Peng, F. Hu, L. Li, H.-Y. Chen, J. Wang and S. Peng, *Angew. Chem. Int. Ed.*, 2023, **62**, e202311937.
  18. H. Li, W. Wang, S. Xue, J. He, C. Liu, G. Gao, S. Di, S. Wang, J. Wang, Z. Yu and L. Li, *J. Am. Chem. Soc.*, 2024, **146**, 9124-9133.
  19. D. Xiong, X. He, Z. Zhu, T. Liu, D. Wu, Y. Zou and Z. Chen, *Adv. Funct. Mater.*, 2025, DOI: 10.1002/adfm.202518434, e18434.



20. Z. Tu, X. He, X. Liu, D. Xiong, J. Zuo, D. Wu, J. Wang and Z. Chen, *Chinese J. Catal.*, 2024, **58**, 146-156.
21. H. Yang, J. Dong, X. Gao, C. Ni, Z. Li, Y. Liu, J. Li, X. He, W. Tan, L. Feng and L. Tian, *Small*, 2025, **21**, 2410399.
22. B. C. Bayer, D. A. Bosworth, F. B. Michaelis, R. Blume, G. Habler, R. Abart, R. S. Weatherup, P. R. Kidambi, J. J. Baumberg, A. Knop-Gericke, R. Schloegl, C. Baehtz, Z. H. Barber, J. C. Meyer and S. Hofmann, *J. Phys. Chem. C*, 2016, **120**, 22571-22584.
23. X. Chen, C. Chen, M. M. Amjad, D. Sun, B. Sun and K. Zhang, *Appl. Catal. B-Environ.*, 2024, **344**, 123644.
24. C. Griesser, S. Diaz-Coello, M. Olgiati, W. F. do Valle, T. Moser, A. Auer, E. Pastor, M. Valtiner and J. Kunze-Liebhäuser, *Angew. Chem. Int. Ed.*, 2025, **64**, e202500965.
25. L. Deng, S.-F. Hung, Z.-Y. Lin, Y. Zhang, C. Zhang, Y. Hao, S. Liu, C.-H. Kuo, H.-Y. Chen, J. Peng, J. Wang and S. Peng, *Adv. Mater.*, 2023, **35**, 2305939.
26. S. Gong, B. Ni, X. He, J. Wang, K. Jiang, D. Wu, Y. Min, H. Li and Z. Chen, *Energ. Environ. Sci.*, 2023, **16**, 5956-5969.
27. C. Ai, F. Dang, J. Wan, Z. Jiang, Y. Wu, J. Liu, H. Xu, Y. Wang, Y. Jian, M. Tian, C. Chen, Y. Yu and C. He, *ACS Catal.*, 2025, **15**, 7217-7231.
28. X. He, S. Xue, X. Liu, D. Xiong, X. Xiao, D. Wu, J. Wang, Q. Xu and Z. Chen, *Adv. Energy Mater.*, 2025, **15**, 2405473.
29. M. Li, Y. Huang, Q. Luo and Y. Ji, *Phys. Chem. Chem. Phys.*, 2025, **27**, 3206-



- 3216.
30. Z. Li, H. Yang, W. Cheng and L. Tian, *Chin. Chem. Lett.*, 2024, **35**, 109237.
31. S. Barwe, J. Weidner, S. Cychy, D. M. Morales, S. Dieckhöfer, D. Hiltrop, J. Masa, M. Muhler and W. Schuhmann, *Angew. Chem. Int. Ed.*, 2018, **57**, 11460-11464.
32. C. Wang, Z. Zhao, W. Cao, Y. Peng, M. Song and Y. Wu, *Adv. Funct. Mater.*, 2025, **35**, 2502618.
33. H. Zhou, Y. Ren, B. Yao, Z. Li, M. Xu, L. Ma, X. Kong, L. Zheng, M. Shao and H. Duan, *Nat. Commun.*, 2023, **14**, 5621.
34. G. Liu, T. Nie, Z. Song, X. Sun, T. Shen, S. Bai, L. Zheng and Y.-F. Song, *Angew. Chem. Int. Ed.*, 2023, **62**, e202311696.
35. Y. Wan, Y. Tang, Y. Zuo, K. Sun, Z. Zhuang, Y. Zheng, W. Yan, J. Zhang and R. Lv, *Energ. Environ. Sci.*, 2025, **18**, 7460-7469.
36. L. Deng, H. Chen, S.-F. Hung, Y. Zhang, H. Yu, H.-Y. Chen, L. Li and S. Peng, *J. Am. Chem. Soc.*, 2024, **146**, 35438–35448.
37. Y.-H. Wang, Y. Yang, F.-Y. Gao, X.-L. Zhang, L. Zhu, H.-K. Yan, P.-P. Yang and M.-R. Gao, *Angew. Chem. Int. Ed.*, 2024, **63**, e202407613.
38. H. Qin, Y. Ye, G. Lin, J. Zhang, W. Jia, W. Xia and L. Jiao, *ACS Catal.*, 2024, **14**, 16234-16244.
39. J. G. Davis, B. M. Rankin, K. P. Gierszal and D. Ben-Amotz, *Nat. Commun.*, 2013, **5**, 796-802.
40. R. Guo, Y. Zhou, W. Wang, Y. Zhai, X. Liu, W. He, W. Ou, R. Ding, H.-L.



- Zhang, M. Wu, Z. Jiang and K.-G. Zhou, *Sci. Adv.*, 2025, **11**, eadr5374.
41. X. Wang, S. Xi, W. S. V. Lee, P. Huang, P. Cui, L. Zhao, W. Hao, X. Zhao, Z. Wang, H. Wu, H. Wang, C. Diao, A. Borgna, Y. Du, Z. G. Yu, S. Pennycook and J. Xue, *Nat. Commun.*, 2020, **11**, 4647.
  42. P. Ren, T. Gan, J. Cai, J. Hao, Z. Zhuang, C. Jin, W. Zhang, M. Du and H. Zhu, *Angew. Chem. Int. Ed.*, 2025, **64**, e202502776.
  43. Z. Yang, F. Lai, Q. Mao, C. Liu, S. Peng, X. Liu and T. Zhang, *Adv. Mater.*, 2024, **22**, 2412950.
  44. Q. Luo, K. Wang, Q. Zhang, W. Ding, R. Wang, L. Li, S. Peng, D. Ji and X. Qin, *Angew. Chem. Int. Ed.*, 2024, **64**, e202413369.
  45. Z. Li, H. Liu, Y.-H. Wang, S. Ji, Y. Zhang, Y. Liu, X. Lu, H. Teng, J. H. Horton, Y. Wang, X. Ma and Y.-J. Tang, *ACS Nano*, 2024, **19**, 1600–1610.
  46. Y. Ye, J. Xu, X. Li, Y. Jian, F. Xie, J. Chen, Y. Jin, X. Yu, M.-H. Lee, N. Wang, S. Sun and H. Meng, *Adv. Mater.*, 2024, **36**, 2312618.
  47. J. Zhou, Y. Xiong, M. Sun, Z. Xu, Y. Wang, P. Lu, F. Liu, F. Hao, T. Feng, Y. Ma, J. Yin, C. Ye, B. Chen, S. Xi, Y. Zhu, B. Huang and Z. Fan, *Proc. Natl. Acad. Sci. U.S.A.*, 2023, **120**, e2311149120.
  48. X. Yin, W. Sun, K. Chen, Z. Lu, J. Chen, P. Cai and Z. Wen, *Adv. Sci.*, 2024, **11**, 2402343.
  49. Y. Niu, S. Gong, X. Liu, C. Xu, M. Xu, S.-G. Sun and Z. Chen, *eScience*, 2022, **2**, 546-556.





## Data availability statements

View Article Online  
DOI: 10.1039/D5SC09133K

The data supporting this article have been included as part of the Supplementary Information.

